MATERIALS CHEMISTRY
FRONTIERS

RESEARCH ARTICLE

View Article Online
View Journal | View Issue

Cite this: *Mater. Chem. Front.*, 2018, **2**, 2297

New fluorescent columnar mesogens derived from phenanthrene–cyanopyridone hybrids for OLED applications†

D. R. Vinayakumara, [a] Hidayath Ulla, ‡[b] Sandeep Kumar, [c] M. N. Satyanarayan[d] and Airody Vasudeva Adhikari *[a]

Received 31st July 2018,
Accepted 7th October 2018

DOI: 10.1039/c8qm00377g

rsc.li/frontiers-materials

We report the design, synthesis, and self-assembly of a novel series of pseudodiscoid dyads comprising electron-rich dialkoxyphenanthrene and trialkoxyphenyl rings appended to an electron-deficient cyanopyridone core. Evidently, all the members of the series exhibited bi-mesophases with prospective columnar mesomorphism; moreover, it was steady under ambient conditions. The electro-optical studies revealed that the new liquid crystalline materials were efficient green light emitters both in solution and LC states with substantial chromaticity. Further, their theoretical studies (DFT) revealed that the molecules possess good intramolecular charge transport behavior. These superior properties of the LC materials render them to become promising candidates for OLED applications. Their electroluminescence competence was studied by fabricating doped and non-doped simple-architecture OLED devices. One of the doped devices with **Py-2** as the emissive layer exhibits the highest deep-green electroluminescence with a brightness of 1898 cd m^{-2} at 4.23 V having CIE coordinates of (0.312, 0.606).

Introduction

Since the breakthrough discovery of electroluminescence from organic molecules in 1987,[1] organic light emitting diodes (OLEDs) are considered to be the next-generation ecofriendly solid-state lighting technology. This may be attributed to their advantageous features such as low cost; high power efficiency; wide color gamut; ease of fabrication by solution processes; and ability to yield curved, thin, and flexible devices.[2–7] Nevertheless, the current challenges facing this field are the development of ideal light emitting device materials, engineering of device structures, and their optimization to obtain increasingly efficient and long-life devices.[8]

Certainly, the emissive layer is a vital component that determines the overall efficiency of the device. Till today, a large variety of luminescent materials have been developed in order to improve the device performance.[9–17] Presently, one of the major challenges is the development of efficient fluorophores with high charge transport characteristics in addition to preserving the solid-state emission for high-performance non-doped OLEDs. In this context, columnar liquid crystals (CLCs) have proven to be better alternatives to the insulating amorphous solids and expensive single-crystal fluorophores due to their effective combination of π–π self-stacking with long-range order, self-healing ability, easy processability, good luminescence ability, and intrinsic charge carrier property in the soft condensed state.[18–24]

In the columnar phase, molecular discs stack on the top of the other to form columns that self-organize into different lattices. Here, the intracolumnar (core–core) separation of the aromatic discs is usually of the order of 0.35 nm; therefore, there is considerable overlap between the π orbitals. On the other hand, the intercolumnar (column–column) separation is commonly 2–4 nm, depending on the length of the peripheral aliphatic chains. Therefore, intracolumnar interactions between neighboring molecules within the columns are much stronger than intercolumnar interactions. The columnar phase provides a facile path for the movement of charges *via* a hopping process. In CLCs, conductivity along the columns has been observed to be several orders of magnitude higher than that in the perpendicular direction. Time-of-flight charge mobility up to about 0.1 $cm^2\ V^{-1}\ s^{-1}$ has been realized in columnar mesophases. As the mobility of the

[a] *Organic Materials Laboratory, Department of Chemistry, National Institute of Technology Karnataka, Surathkal, Mangalore-575 025, India. E-mail: avachem@gmail.com, avachem@nitk.ac.in*
[b] *Department of Chemistry, Indian Institute of Technology Guwahati, Guwahati-781 039, India*
[c] *SCM Group, Raman Research Institute, C.V. Raman Avenue, Sadashivanagar, Bangalore-560 080, India*
[d] *Department of Physics, National Institute of Technology Karnataka, Surathkal, Mangalore-575 025, India*

† Electronic supplementary information (ESI) available. See DOI: 10.1039/c8qm00377g

‡ H. Ulla designed, executed and analyzed the OLED investigations.

charge carriers is a key factor in determining the device performance (*e.g.*, OLEDs, solar cells, sensors, *etc.*), these materials have promising applications in such optoelectronic devices.[25,26] Therefore, the use of luminescent CLCs as the emissive layer in OLEDs can enhance the device performance due to their high charge carrier mobility caused by the long-range order along with their intense luminescence properties. Hence, CLC-based OLEDs can be used as a potential backlight for liquid crystal displays (LCDs) by replacing the expensive backlight and absorbing color filters, which correspondingly reduces the overall cost of the device and significantly enhances the emission efficiency.[27–29] In this context, considerable efforts have been focused on developing luminescent liquid crystals with decent charge mobility and employing them as active components in fabricating electroluminescent devices.

Recently, few OLEDs comprising columnar fluorescent materials as the sole emissive layer and/or as an emissive dopant ensued with noticeable external quantum efficiency have been reported.[27,30–33] In CLCs, notorious aggregation-caused quenching effect is a common occurrence, mainly due to the principal intermolecular interactions at the ordered arrangements of the molecules. In order to maintain the significant exciton emission in the mesophase, various molecular designs have been explored.[34,35] Among the most successful designs, employing the donor–acceptor (D–A) moieties in the core structure was found to be an excellent approach; therefore, easy tailoring of essential optical and electrochemical properties is possible. Moreover, the proper selection of donor and acceptor scaffolds is important in order to ensure their efficient D–A interactions, subsequently influencing the intramolecular charge transfer (ICT) property, and hence, tuning the HOMO–LUMO energy bandgap.

On the basis of our continuous effort in this context,[36–40] we have rationally designed a new class of nonsymmetrical D–A–D-structured mesogens, **Py-1** to **Py-3**, for OLED applications. In the new design, π-rich 9,10-didodecyloxyphenanthrene and trialkoxybenzene units have been selected as effective electron donors, while 3-cyanopyridone moiety as an efficient electron acceptor to achieve optimum optoelectronic properties at the liquid crystalline state (Fig. 1). It is expected that mesogens containing a phenanthrene core, because of its polycyclic aromatic hydrocarbon (PAH) structure, may possess good self-assembling property with effective π-orbital overlapping, which, in turn, reduces the intercolumnar spacings yielding good charge migration ability through the columnar stack. Moreover, the introduction of additional alkoxy donors in electron-rich phenanthrene attached to electron-deficient cyanopyridone offers efficient D–A interactions. Consequently, the designed mesogens would exhibit necessary optoelectronic properties for their use in OLED devices. In the present work, all the final compounds (**Py-1** to **Py-3**) were synthesized through simple and efficient synthesis protocols. They were effectively characterized using different spectral techniques. Their mesomorphic, photophysical, electrochemical, and theoretical studies were comprehensively undertaken. Finally, we investigated their electroluminescence ability as emitting materials by fabricating multilayer OLED device structures.

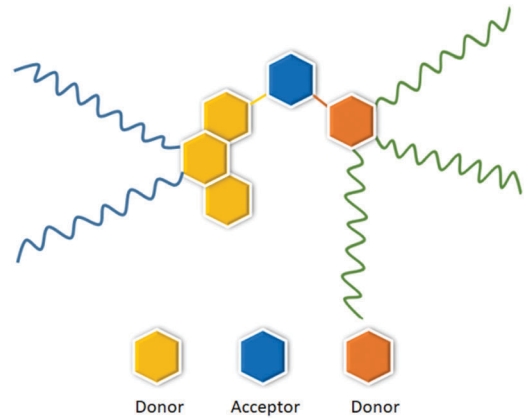

Fig. 1 Nonsymmetrical structural design of new mesogens.

Results and discussion

Synthesis and characterization

The designed chemical structures and synthetic routes for the target compounds, **Py-1** to **Py-3**, are shown in Scheme 1. Firstly, 9,10-phenanthrenequinone (**1**) was reduced with $Na_2S_2O_4$ followed by alkylation using a phase transfer catalyst, Bu_4NBr, in 1 : 1 THF and H_2O mixture to yield 9,10-didodecyloxyphenanthrene (**2**). Compound **2** was subjected to Friedel–Crafts acetylation with 1 equivalent of acetyl chloride under controlled conditions to exclusively give monoacetylated product **3** in a good yield. All the required 3,4,5-trialkoxybenzaldehydes **7a–c** were prepared through a multistep synthesis process by adopting the reported procedures.[41] Finally, the condensation of acetyl derivative **3** and different aldehydes **7a–7c** with ethyl cyanoacetate yielded the target mesogenic compounds, **Py-1** to **Py-3**. All the intermediate and final compounds were characterized by FTIR, ^{1}H-NMR, and ^{13}C-NMR spectral and elemental analyses. Their spectra are furnished in the ESI.†

Self-assembling properties

The thermotropic phase behaviors of all the new cyanopyridone derivatives, **Py-1** to **Py-3**, were studied by differential scanning calorimetry (DSC) and cross-polarized optical microscopy (POM) techniques. Further, the molecular self-assembly in different mesophase structures was determined by means of variable-temperature X-ray diffraction (XRD) experiments. The resultant phase transition temperatures and associated energy changes are summarized in Table 1. Evidently, all the three compounds were found to exhibit enantiotropic mesophase behavior at room temperature, which stabilized over a wide temperature range with relatively lower isotropization points.

The DSC thermograms of **Py-1** to **Py-3** are shown in Fig. 2a–c. Apparently, the DSC trace of compound **Py-1** did not show any signs of melting on the heating scan; instead, it displayed two distinct transitions at 89.48 °C and 104.30 °C with smaller enthalpy changes of 1.09 kJ mol^{-1} and 0.20 kJ mol^{-1} due to LC–LC and LC–I transitions, respectively (Fig. 2a). In the cooling cycle, both the transition peaks reoccurred at 96.10 °C and 75.52 °C without any crystallization transitions till reaching

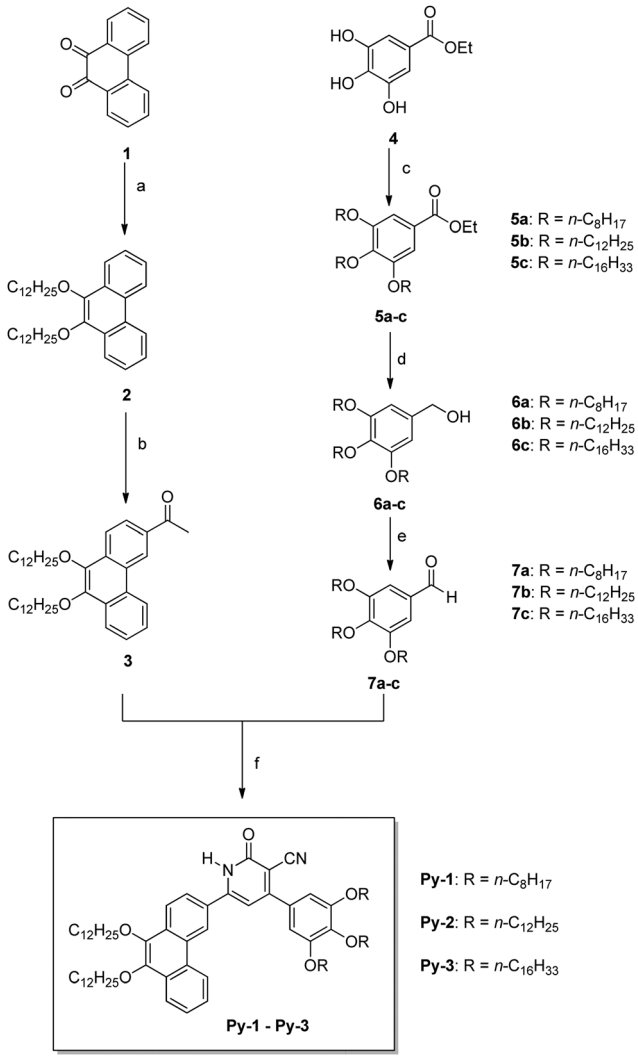

Scheme 1 *Reagents and conditions*: $Na_2S_2O_4$, KOH, Bu_4NBr, $C_{12}H_{25}Br$, 1 : 1 H_2O, and THF, RT, 48 h, 75%; (b) CH_3COCl, $AlCl_3$, DCM, −5 to 25 °C, 1 h, 80%; (c) K_2CO_3, KI, *n*-RBr, DMF, 75 °C, 12 h, 69–85%; (d) $LiAlH_4$, anhydrous THF, −10 to 25 °C, 16 h, 83–92%; (e) PCC, dry DCM, 3 h, 80–63%; (f) ethyl cyanoacetate, ammonium acetate, EtOH, 70 °C, 16 h, 25–36%.

room temperature. The perceived very low enthalpy changes may be attributed to the highly fluidic nature of the mesophases. Compound **Py-2** carrying longer alkyl chains also showed two separate mesophases at a relatively higher temperature, having a clearing point at 132.95 °C than that of **Py-1**. On cooling, both the LC phases reappeared and did not exhibit any signals of crystallization, as shown in Fig. 2b. Further, analog compound **Py-3** bearing much longer terminals (hexadecyloxy) displayed two clear mesomorphic states at 121.19 °C (Fig. 2c). It was observed that this set of compounds has not shown any regular trend in their mesophase thermal stability despite the fact that there exists a linear increase in the alkyl chain length in the phenyl arm.

Under POM, a highly birefringent mosaic pattern was observed upon the slow cooling of compound **Py-1** from its isotropic state, which was high fluidic and shearable even at room temperature (Fig. 3a and b). This is a typical indication of the existence of columnar mesomorphism.[25] Moreover, upon cooling down from the higher temperature mesophase to its lower one, a remarkable decline in the optical birefringence was noticed in some of the bright areas, as shown in Fig. 3a and b, which may be due to the inter and/or intracolumnar transitions. The observed optical textural changes were fairly consistent with the DSC transitions. However, in the case of **Py-2**, dendritic growth appeared initially, which, in turn, formed a typical mosaic pattern at the lower temperature LC phase and it remained unchanged until the temperature was reduced to much lower values (Fig. 3c and d). As seen in Fig. 3d and e, compound **Py-3** displayed similar characteristic optical textures for columnar phases featuring a combination of mosaics with linear and fan-shaped birefringent defects as well as homeotropic regions. The POM images of **Py-1** to **Py-3** captured in both the mesophase ranges are shown in Fig. 3a–f.

In order to obtain further insights into the self-organization of the molecules in the different mesophase structures, powder XRD studies were carried out for non-aligned samples of all the new mesogens. As indicated by the DSC traces, they were found to be bi-mesomorphic in nature. Definitely, the XRD patterns gained for **Py-1** in both the LC phase ranges were fairly different; indeed, they are almost similar within their respective mesophase range at different temperature points (Fig. 4a and b). For instance, the XRD trace at 90 °C (within the higher temperature mesophase range) showed two sharp reflections in the lower angle region in the reciprocal ratio of $1:\sqrt{3}$. However, in the wide angle region, a rather diffused halo was observed at 4.39 Å, similar to the liquid-like aliphatic chains (Fig. 4a). The observed two lower angle signals can be assigned to the (10) and (11) planes with hexagonal symmetry for a = 30.41 Å. In fact, only these reflections do not unambiguously confirm the formation of a hexagonal lattice. Nevertheless, such observations are frequent in hexagonal mesophases bred by diverse mesogenic structures.[42–49] This may be due to the minimum in the form factor, which prevents the appearance

Table 1 Phase transition temperatures (°C) and the corresponding energy changes[a] (kJ mol^{-1})

	Phase sequence	
Compound	Heating	Cooling
Py-1	Col_r 89.48 (1.09) Col_h 104.30 (0.20) I	I 96.1 (−0.50) Col_h 75.52 (−1.12) Col_r
Py-2	Col_r 112.20 (2.36) Col_h 132.95 (2.04) I	I 130.80 (−1.21) Col_h 101.0 (−2.37) Col_r
Py-3	Col_r 73.69 (0.24) Col_h 121.19 (1.41) I	I 116.20 (−1.08) Col_h 55.10 (−0.19) Col_r

[a] Peak temperatures, °C (enthalpy/kJ mol^{-1}) obtained by second heating and first cooling at the rate of 5 °C min^{-1}; Col_r = columnar rectangular phase; Col_h = columnar hexagonal phase; I = isotropic liquid phase.

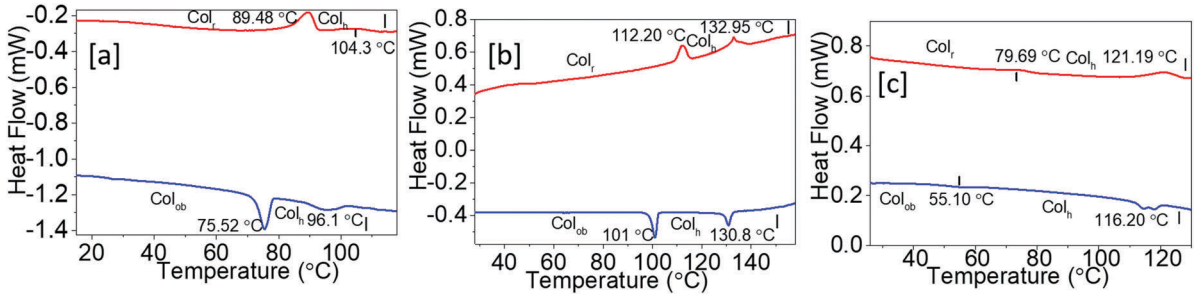

Fig. 2 DSC thermograms: (a) **Py-1**; (b) **Py-2**; (c) **Py-3** (red and blue traces represent second heating and first cooling cycles, respectively).

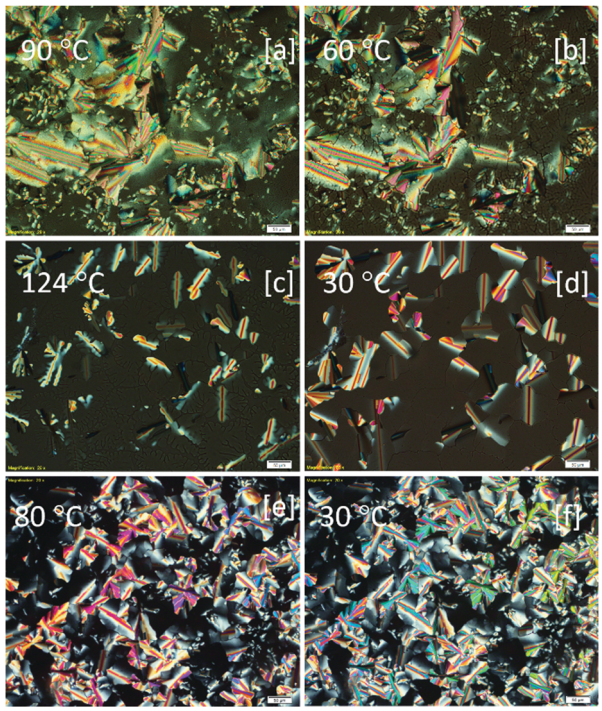

Fig. 3 Optical images captured for **Py-1** to **Py-3** under cross-POM upon slow cooling from their respective isotropic phase: (a) at 90 °C and (b) at 60 °C for **Py-1**; (c) at 124 °C and (d) at 30 °C for **Py-2**; (e) at 80 °C and (f) at 30 °C for **Py-3**.

of peaks in the lower angle region. Moreover, the appearance of typical optical textures confirm the presence of a columnar hexagonal phase. The lattice area S and molecular volume V were estimated to be 801 Å^2 and 3517 Å^3, respectively.

The XRD pattern of the lower temperature mesophase range (obtained at room temperature) showed a number of reflections in the lower angle region (Fig. 4b). In addition, a broad halo centered at 4.43 Å due to alkyl chain correlations was observed. The set of signals are assigned to the (01), (11), (21), (30), (31), and (32) diffractions of the rectangular lattice with the unit cell parameters a = 33.86 Å and b = 26.01 Å.

Similarly, the XRD patterns were obtained at discrete temperatures in both the mesophase ranges of **Py-2**, as shown in Fig. S22 (ESI†). Evidently, the patterns obtained at 128 °C and 115 °C reveal that the reciprocal d-spacings of the lower angle reflections are in the ratio of $1:\sqrt{3}$ and they can be attributed to the (10) and (11) planes of the hexagonal lattice. Their lattice parameters were calculated to be 32.34 and 32.36 Å, respectively. However, the XRD pattern at the lower temperature mesophase of **Py-2** (obtained at 25 °C) revealed a set of reflections that can be certainly assigned to the columnar rectangular phase because a = 33.79 Å and b = 27.72 Å (Fig. S22, ESI†). Similarly, mesogen **Py-3** adopted the Col$_r$ and Col$_h$ phases at lower and higher temperatures, respectively, as shown in Fig. S23 (ESI†). A detailed XRD index is summarized in Table 2. From these results, it is evident that no generic trend was noticed in the thermal stability of mesophases in spite of the systematic sequential variations in the lengths of the peripheral chains. Therefore, mesophase types and ranges are independent of the terminal chain lengths in these molecules. This may be due to numerous structural conformations of the two arms with lengthy flexible chains of the central cyanopyridone core. However, all the compounds have organized into similar mesophases with two different lattice structures.

The obtained results indicated that all the members of the series displayed two distinct columnar mesophases as a function temperature. Compound **Py-2**, with the critical chain length among the series, was selected to be the representative example to understand the molecular assembly in the mesomorphic states. Initially, the number of molecules occupied in each columnar stratum (Z) was estimated by assuming the density equal to 1 g cm^{-3}.[50] Accordingly, nearly two molecules are involved in each columnar slice of both the mesophases to ensure that the space is filled by the disc-like structure. It should be noted that the central cyanopyridone core, capable of forming closed-type H-bonding, may stabilize the dimeric unit through strong intermolecular H-bonding.

As evident from many classical and unconventional discotic materials, all the compounds showed a thermodynamic intercolumnar transition from rectangular to hexagonal columnar assemblies, which was exhibited by the observed small enthalpy changes, optical variations, and differences in XRD patterns.[51] Further, the dimeric structures form a columnar array with rectangular and hexagonal symmetries, wherein the position of the molecules is not fixed; in fact, it is truly liquid-like. This may be attributed to its propeller-like structures whose conformational motions increase the mesogenic fluctuations and intracolumnar tilting, which could be responsible for the disappearance of the core–core peak in the XRD pattern for Col$_h$. This type of mesophase is sometimes termed as "disordered columnar mesophases"

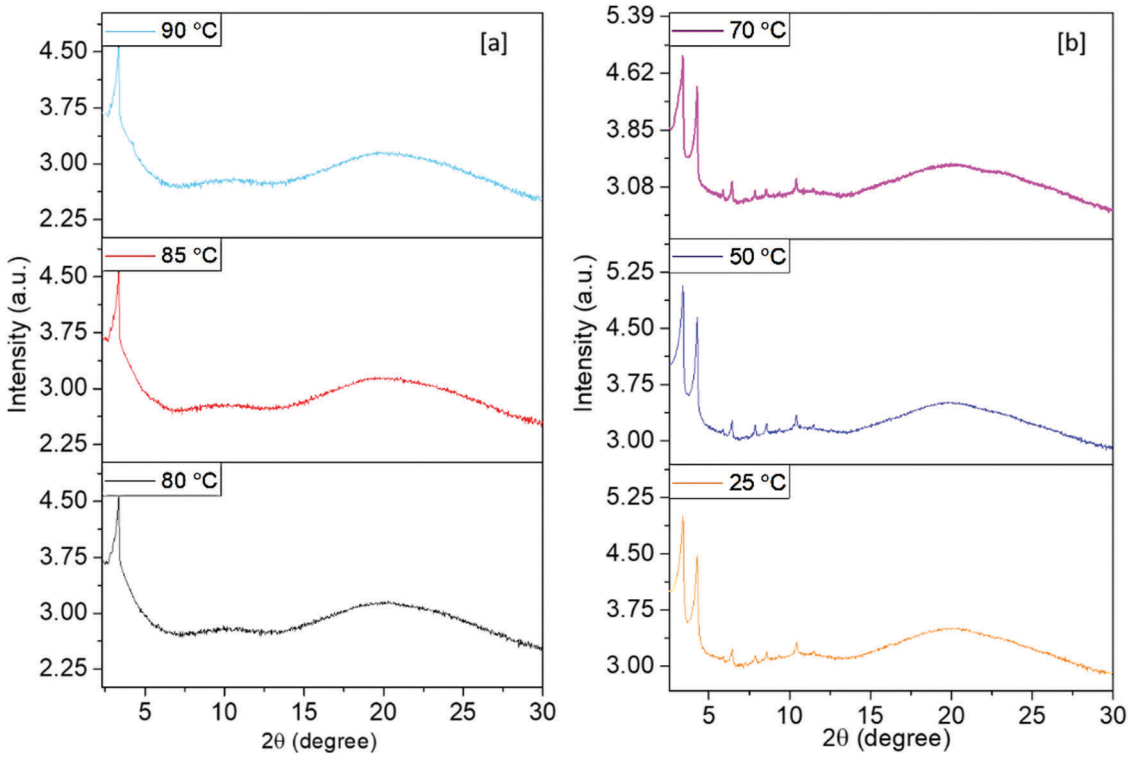

Fig. 4 XRD patterns obtained for **Py-1** at various temperatures in the (a) higher and (b) lower temperature mesophase ranges.

in order to distinguish from the ordered assemblies.[52] However, these molecules may possess some degree of order due to the intermolecular H-bonding along the columnar axis through the central ring. In addition, its D–A–D core structure would also stabilize the mesophase by strong intracolumnar D–A interactions. Considering these facts, we proposed a schematic model for the molecular self-assembly of **Py-2** in Col_r and Col_h with plausible H-bonding interactions (Fig. 5).

Photophysical properties

The suitability of the newly synthesized LC materials for OLED device fabrication was established by examining their electronic absorption and emission spectra. The UV-visible and fluorescence spectra were recorded in dichloromethane at $c = 2 \times 10^{-5}$ M. Structurally, all the members of the series differ only in the length of the saturated alkyl chains, which usually causes a negligible effect on their optoelectronic properties. Consequently, all the compounds displayed similar characteristic absorption and emission spectra. They showed three distinct absorption maxima, namely, a strong band at ~258 nm, a weak peak at ~300 nm, and a prominent maxima centered at ~395 nm, as shown in Fig. S24 (ESI†). The first two bands arise due to the π–π* transitions and the longer wavelength absorption band is attributed to the ICT from dialkoxyphenthrene and trialkoxybenzene donors to the cyanopyridone acceptor. On exciting at their respective longest absorption wavelengths, they exhibited a single emission band at ~502 nm with relatively higher Stokes shift values in the range of 5396–5420 cm^{-1}. The observed large Stokes shift signifies the effective ICT property in these π-conjugated structures, and it is the most advantageous characteristic for a desirable emitter in the fabrication of OLEDs. The optical bandgaps were calculated using the onset wavelength of the absorption peak and they were found to be in the range of 2.72–2.75 eV. For an ideal fluorophore, fluorescence quantum yield (Φ_F) is one of the deciding factors. In view of this, their absolute solution photoluminescence (PL) quantum yields were estimated, and they were found to be noticeably high in the range of 0.48–0.52. The detailed optical data are summarized in Table 3.

The fluorescence lifetime of new mesogenic materials was estimated for the DCM solution samples ($c = 2 \times 10^{-5}$ M) using the TCSPC technique by probing at their respective emission maxima. The resultant fluorescence kinetic decay profiles are shown in Fig. 8a. The traces fitted with the biexponential decay showed average lifetime values of 2.54 ($\chi^2 = 1.0$), 2.51 ($\chi^2 = 0.99$), and 2.51 ($\chi^2 = 1.01$) for **Py-1**, **Py-2**, and **Py-3**, respectively (Table 3). The same samples were illuminated under a longer wavelength and their photographs are shown in Fig. 6b. To investigate the PL behavior of these materials at the liquid crystalline state, their neat thin films were prepared by the spin coating technique and the fluorescence spectra were obtained by exciting them at their respective solution absorption maxima (Fig. 6c). Interestingly, the emission wavelength (504–508 nm) exhibited marginal shifts when compared to the solution emission maxima (501–502 nm). A visually perceivable emission was observed under light illumination of 365 nm, as shown in Fig. 6d.

Further, the effect of solvent on the optophysical properties of these emitting LC materials was examined by studying the absorption and emission characteristics of a representative

Table 2 XRD data of **Py-1** to **Py-3**

Compd	Phase (T/°C)	d_{obs} [Å]	d_{cal} [Å]	Miller indices (hk)	Lattice parameter a [Å], lattice area S [Å^2], cell volume V [Å^3]
Py-1	Col_h (90)	26.34	26.03	(10)	a = 30.41
		15.15	15.20	(11)	S = 801.1
		4.39 (h_a)			V = 3516.9
					Z = 1.88
	Col_r (25)	26.01	26.01	(10)	a = 33.86
		20.60	20.59	(11)	b = 26.01
		13.80	14.18	(21)	S = 880.7
		11.13	11.28	(30)	V = 3901
		10.22	10.35	(31)	Z = 2.08
		8.45	8.50	(32)	
		4.43 (h_a)			
Py-2	Col_h (115)	28.03	28.03	(10)	a = 32.36
		16.13	16.18	(11)	S = 907.2
		4.48 (h_a)			V = 4064
					Z = 1.89
	Col_r (25)	27.72	27.72	(01)	a = 33.79
		21.43	21.43	(11)	b = 27.72
		15.99	16.89	(20)	S = 936
		14.51	14.43	(21)	V = 3587
		12.79	12.82	(12)	Z = 1.66
		8.88	8.91	(13)	
		3.83 (h_c)			
		4.40 (h_a)			
Py-3	Col_h (80)	30.05	30.05	(10)	a = 34.69
		17.29	17.34	(11)	S = 1042
		4.45 (h_a)			V = 4645.5
					Z = 1.91
	Col_r (25)	29.66	29.66	(01)	a = 34.06
		22.37	22.36	(11)	b = 29.66
		17.13	17.03	(20)	S = 1010
		15.25	14.83	(02)	V = 4424
		13.58	13.59	(12)	Z = 1.82

d_{obs}, observed spacings; d_{cal}, calculated spacings; h_a, alkyl chains correlation peak value; h_c, π–π spacing; Z, number of molecules per columnar slice. Alkyl halo was considered for the calculations when the core–core peak is absent.

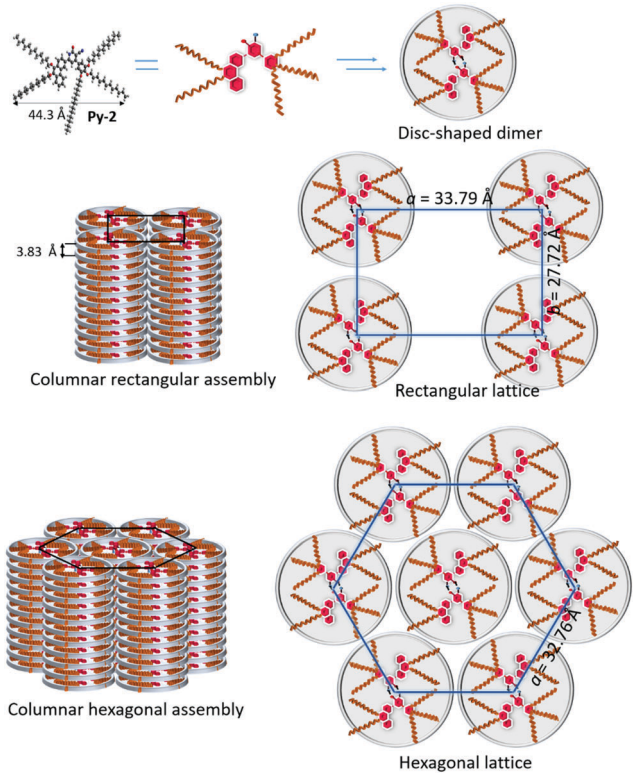

Fig. 5 Schematic model showing the energy-minimized structure of **Py-2** (obtained by MM2 method) and its self-assembly in Col_h and Col_r phases with plausible H-bonding (XRD data at 115 °C and 25 °C were used for the illustration).

Table 3 Photophysical characterization data of **Py-1** to **Py-3**

Compd	λ_{abs} (nm)	λ_{em} (nm)	Stokes shift (cm^{-1})	$E_{g\,opt}$ (eV)	$\lambda_{em}{}^a$ (nm)	$\Phi_F{}^b$	τ^c (ns)	τ_1/τ_2
Py1	259, 302, 394	501	5420	2.72	504	0.52	2.39/4.31	
Py2	258, 300, 395	502	5396	2.73	506	0.49	2.41/4.61	
Py3	258, 300, 395	502	5396	2.75	508	0.48	2.28/3.71	

[a] Estimated for thin films. [b] Absolute quantum yield determined using an integrated sphere. [c] Fluorescence lifetime at the excitation wavelength, λ_{exc} = 350 nm.

compound, namely, **Py-1**. Its UV-visible and fluorescence spectra are shown in Fig. S25 (ESI†), and the relevant data are compiled in Table S1 (ESI†). Evidently, the absorption profile showed a lack of solvent dependence, indicating a nonpolar ground state. However, a slight red-shift in the emission bands on the increasing solvent polarity demonstrated the trivial positive fluorescence solvatochromism. Notably, the unusual bathochromic shift perceived in the DCM arises due to the effective solvation in the solvent induced by the instant stabilization of polarizable electrons during electronic excitation.[53]

Conclusively, the observed larger Stokes shift, biexponential PL decay, and nonlinear solvatochromic shift indicated the existence of locally excited (LE), as well as charge transfer (CT), states in these D–A–D luminogens. In addition, density functional theory (DFT) calculations reveal a slight twist in the donor moieties with respect to the central acceptor core, suggesting that the second exciton species might have arisen due to the twisted intramolecular charge transfer (TICT).[54] This type of coexistence of LE and CT characteristics is generally called the "hybridized local and charge transfer" (HLCT) state, which is known to contribute toward the enhancement of fluorescence radiative decay, which improves the electroluminescence efficiency of OLEDs.[55–57]

Electrochemical properties

The electrochemical process and energy levels of frontier molecular orbitals (FMOs) in these new cyanopyridone derivatives were studied by means of the cyclic voltammetry (CV) technique using a standard three-electrode electrochemical cell. For the experiments, the compounds were dissolved in degassed dry DCM (c = 1 × 10^{-3} M) with a TBAP-supporting electrolyte. All the three compounds showed irreversible oxidation and reduction waves at the onset in the range of −1.41 to −1.45 V and −0.83 to −0.87 V, respectively. Accordingly, the energy of the HOMO and LUMO levels were estimated. The obtained electrochemical HOMO–LUMO energy bandgaps (2.28–2.32 eV) are in good agreement with

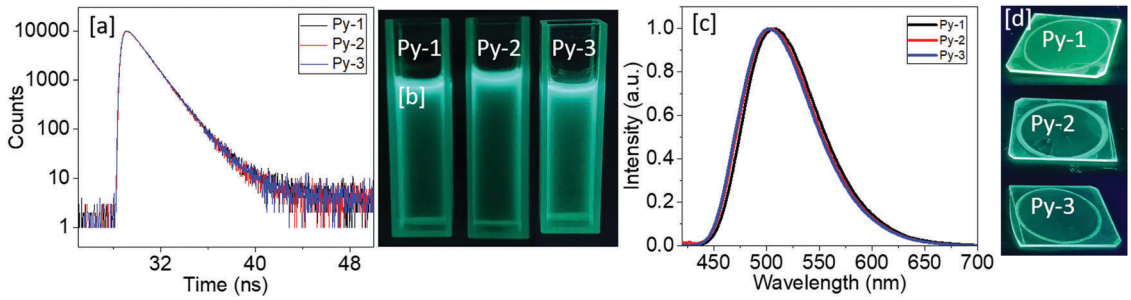

Fig. 6 (a) Fluorescence decay profiles obtained for DCM solution and (b) their emission hue; (c) fluorescence spectra obtained for thin films and (d) their emission hue.

Table 4 Electrochemical characterization of **Py-1** to **Py-3**

Compd	E_{1red} [a] (V)	E_{1oxd} [b] (V)	E_{LUMO} [c] (eV)	E_{HOMO} [d] (eV)	$E_{g\,CV}$ [e] (eV)	$E_{g\,opt}$ [f] (eV)
Py1	−0.83	1.45	−3.46	−5.74	2.28	2.72
Py2	−0.87	1.44	−3.41	−5.73	2.32	2.73
Py3	−0.86	1.41	−3.43	−5.70	2.27	2.75

[a] Onset potential of the first reduction wave. [b] Onset potential of the first oxidation wave. [c] $E_{LUMO} = -[4.8 - E_{1/2,Fc/Fc^+} + E_{1red}]$ eV. [d] $E_{HOMO} = -[4.8 - E_{1/2,Fc/Fc^+} + E_{1oxd}]$ eV, where $E_{1/2,Fc/Fc^+}$ was found to be 0.51 V. [e] $E_{g\,CV} = E_{LUMO} - E_{HOMO}$. [f] Optical bandgap.

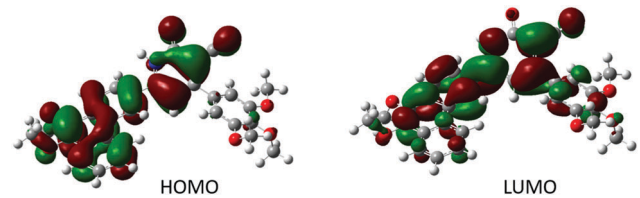

Fig. 7 Simulated optimized geometry, HOMO, and LUMO of the model structure.

the optical bandgaps (2.72–2.75 eV). The recorded CV curves are shown in Fig. S27–S30 (ESI†), and the subsequent electrochemical data are given in Table 4.

To study the FMO distributions in these new molecules, DFT calculations were performed using GAUSSIAN-09 program with the Becke's three-parameter functional and Lee, Yang, and Parr correlation (DFT-B3LYP). In the simulation study, the longer alkoxy chains are replaced by methoxy groups in the model molecular structure to reduce computational time and cost. We presumed that reducing the length of the alkyl chains would not affect the required energy parameters. Its geometrically optimized structure was obtained by using the basic set 6-311G(d,p) (Fig. S24, ESI†). The corresponding simulated energy-minimized structure and HOMO–LUMO levels are shown in Fig. 7. Apparently, both dialkoxyphenanthrene and trialkoxyphenyl rings are not coplanar with the central cyanopyridone core, which resulted in a bowl-shaped structure. As shown in Fig. 7, the HOMOs are concentrated over the dialkoxyphenanthrene and cyanopyridone rings, while LUMOs are delocalized throughout the molecule. These results confirm the presence of a moderate ICT behavior, which validates the experimental electro-optical studies.

Electroluminescence properties

The visually pursuable highly intense emissions at the beneficial room temperature columnar mesophases and admirable redox properties owing to the favorable HOMO–LUMO energy levels make the new LC materials good emitters for OLEDs. In the device study, a typical material, **Py-2**, was employed as the sole emissive material, as well as an emissive dopant material, with three different device architectures. The schematic illustration of the different device structures and the energy level diagram of the materials used in the device are shown in Fig. 8. The device structures are as follows:

Device **I**: ITO/PEDOT:PSS/**Py-2**/LiF/Al.

Device **II**: ITO/PEDOT:PSS/PVK:**Py-2**/LiF/Al.

Device **III**: ITO/PEDOT:PSS/PVK:**Py-2**/BCP/Alq_3/LiF/Al.

In case of device **I**, **Py-2** acted as the sole emissive material; however, in devices **II** and **III**, 10 wt% of **Py-2** doped in the host poly(9-vinylcarbazole) (PVK) served as the emissive material. In the device fabrication, we used patterned indium tin oxide (ITO)-coated glass substrate as a transparent anode. Moreover, poly(3,4-ethylenedioxy-thiophene)/poly(styrene-sulfonate) (PEDOT:PSS) was used as the hole-injection material, which can also facilitate the smoothening of the ITO surface, thereby reducing the turn-on voltage and probability of electric shorts. This, in turn, extends the lifetime of the device.[58,59] PVK possesses the ability to form excellent films and it also has good miscibility with numerous emitting materials. Hence, it was selected as the host material in device configurations **II** and **III**. Bathocuproine (BCP) served as the hole-blocking material (HBM) to restrict the holes from moving toward the emitting layer, whereas tris-(8-hydroxyquinoline)aluminum (Alq_3) functioned as the electron-transport material (ETM) to assist electron injection into the emitting layer. For facilitating electron injection, a bilayer cathode comprising lithium fluoride (LiF) and aluminum (Al) was used in the device structures; here, LiF acts as the electron injection material. Table 5 summarizes the key performance data of the newly fabricated LC-based OLEDs.

Fig. 8c shows the *J*–*V*–*L* features of the fabricated OLEDs. Device **I** comprising only **Py-2** as the emissive material showed low luminance (L_{max}) of 258 cd m^{-2} with current efficiency (η_c) of 0.44 cd A^{-1}, power efficiency (η_p) of 0.12 lm W^{-1}, and external quantum efficiency (η_{EQE}) of 0.29% at 100 cd m^{-2}. Further, the high drive voltage (V_{onset}, 1 cd m^{-2}) of the device

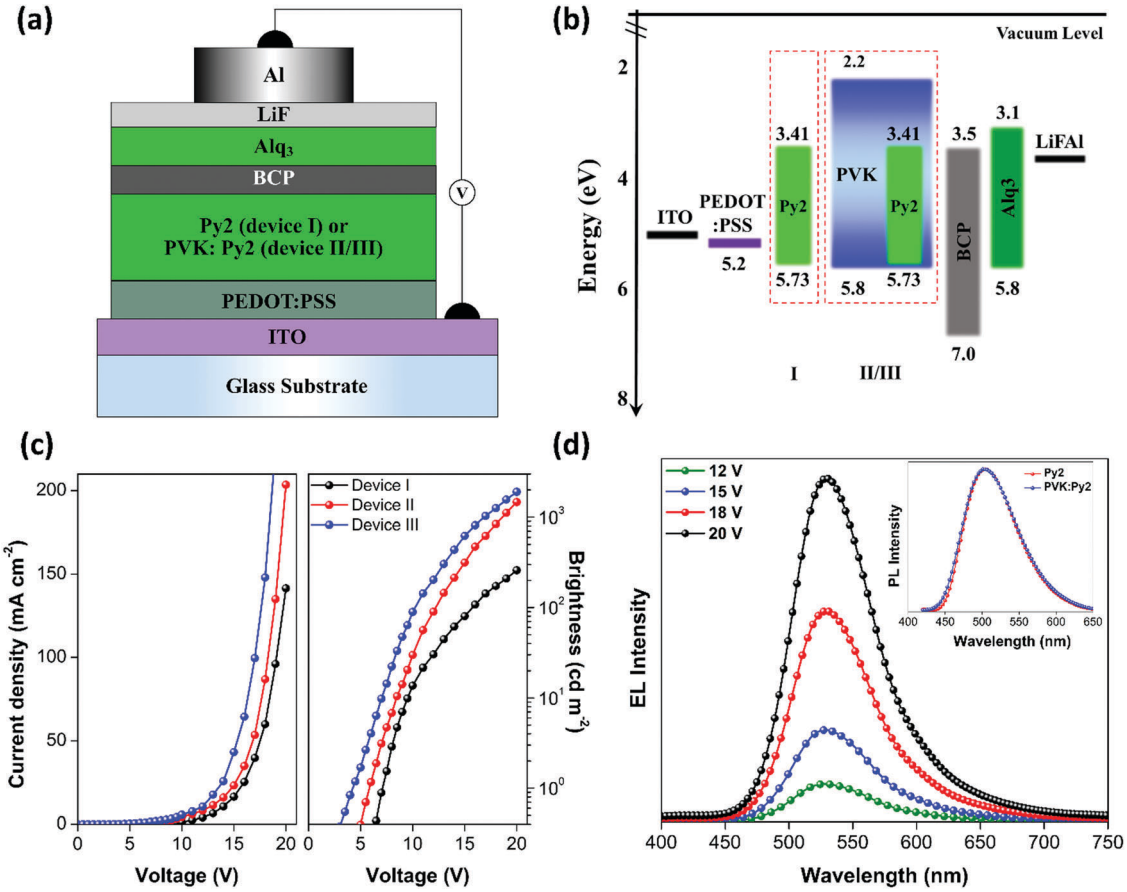

Fig. 8 (a) Schematic of different OLED architectures showing the ITO anode and PEDOT:PSS as the hole-injection material, active luminescent layer, BCP as HBM, Alq_3 as ETM, and LiF:Al as bilayer cathode. (b) Energy-level diagram, giving the approximate ionization energies and electron affinities of the materials used in OLEDs. (c) *J*–*V*–*L* characteristics. (d) EL spectra of device **III** at different bias voltages (inset shows the PL spectra of **Py2** and PVK:**Py-2** thin films).

Table 5 Electroluminescence performance data of new OLEDs

Device	V_{onset} [a] (V)	L_{max} [b] (cd m^{-2})	η_c [c] (cd A^{-1})	η_p [d] (lm W^{-1})	η_{EQE} [e] (%)
I	7.07	258	0.44	0.12	0.29
II	5.79	1463	1.33	0.38	0.73
III	4.23	1898	1.65	0.66	0.98

[a] V_{onset}, turn-on voltage at luminance of 1 cd m^{-2}. [b] Luminance at 20 V. [c] Current efficiency. [d] Power efficiency. [e] External quantum efficiency at 100 cd m^{-2}.

was found to be as high as 7.07 V. However, drastic enhancement in the device performance was observed in which PVK:**Py-2** (10 wt%) was used as the emitting composite (device **II**). The increase in the performance of device **II** can be ascribed to the fact that there is an effective transfer of the exciton energy from PVK (host material) to **Py-2** (emissive dopant).[58,59] Although device **II** showed superior performance as compared to device **I**, it still exhibited a high V_{onset} value (5.79 V), indicating the presence of high charge injection barriers in the device. A balanced flow of charge carriers (electrons and holes) is important to obtain maximum recombination, which eventually will result in improved performance of the devices as the imbalanced charge transport in the emissive layer hampers the performance of the device. Hence, to further improve the device performance and reduce the drive voltage, BCP and Alq_3 were used as HBM and ETM, respectively which is designated as device **III**. Consequently, device **III** showed an improvement in the device performance (L_{max} of 1898 cd m^{-2}, η_c of 1.65 cd A^{-1}, η_p of 0.66 lm W^{-1}, and η_{EQE} of 0.98%) with a significant reduction in V_{onset} (4.23 V) as compared to device **II**. The improved device performance can be attributed to the effective transfer of exciton energy from PVK (host) to **Py-2** (dopant) as well as the balanced charge transport in the emissive layer.[60–62] Further, the use of BCP as HBM assisted in confining the reductant holes in the emitting layer, which did not recombine with the electrons in the emitting zone.[62–65]

All the fabricated OLEDs emitted green light when ITO was positively biased. Fig. 8d shows the EL spectra of the devices at 20 V with the peak at ~531 nm and FWHM of ~72 nm. From Fig. 8d (inset), it is evident that the thin-film PL spectra of PVK and PVK:10 wt% **Py-2** exactly overlap with each other, revealing that both originate from the same excited state. In addition, the shapes of the EL spectra of the devices were similar to the thin-film PL spectra of PVK:**Py-2** (Fig. 8d), which is also due to the same excited state origin. The devices demonstrated excellent

spectral stability as the EL spectra, over a wide range of operating voltages, did not show any changes in the shapes and peaks. This also indicates that during device operation, **Py-2** exhibits excellent thermal stability. The CIE chromaticity coordinates determined using the EL spectra of the OLEDs at 20 V are (0.312, 0.606) corresponding to green emission. It is noteworthy that the investigated OLEDs are unoptimized. Further optimizations can improve the device performance. The results reveal that these phenanthrene–cyanopyridone-based emissive LC materials have promising potential in OLED applications with further scope for improvement in molecular design and device architecture.

Conclusions

In summary, we have rationally designed and synthesized three new D–A–D-configured thermotropic CLC compounds, **Py-1** to **Py-3**, as potential luminescent materials for OLED device applications. The systematic studies explored their supramolecular bi-columnar mesomorphism nature; the mesophase is stable even under ambient conditions. The XRD results revealed that these half-disc-shaped molecules self-assembled into disc-like dimeric structures that further organized into Col_h and Col_r as a function of temperature. The mesophase thermal stability has been noted to be independent of the linear increase in the peripheral chain length at one of the arms. Obviously, all the new LC materials demonstrated a deep and intense green emission in the self-assembled state with the ionization potential and electron affinity in the range of −5.70 to −5.74 eV and −3.41 to −3.46 eV, respectively. Further, their electroluminescence performance was examined by fabricating the solution-processed host–guest OLED devices using the representative compound, *i.e.*, **Py-2**, as an emissive component. The device revealed that a doped LC-OLED device comprising both HBM and ETM constituents has shown a significant improvement in performance.

Conflicts of interest

There are no conflicts to declare.

Acknowledgements

The authors are thankful to NITK, Surathkal and SCM group, RRI, Bangalore, India, for providing necessary laboratory facilities. The authors are also grateful to Dr Vijayaraghavan for recording the NMR spectra, Mrs K. N. Vasudha for their technical support. H. Ulla acknowledges DST-SERB, India (NPDF Award No. PDF/2016/000711) for the financial support.

References

1 C. W. Tang and S. A. VanSlyke, *Appl. Phys. Lett.*, 1987, **51**, 913–915.
2 N. T. Kalyani and S. J. Dhoble, *Renewable Sustainable Energy Rev.*, 2012, **16**, 2696–2723.
3 W. Brütting, J. Frischeisen, T. D. Schmidt, B. J. Scholz and C. Mayr, *Phys. Status Solidi A*, 2013, **210**, 44–65.
4 A. Buckley, *Organic light-emitting diodes (OLEDs): materials, devices and applications*, Elsevier, 2013.
5 D. J. Gaspar and E. Polikarpov, *OLED fundamentals: materials, devices, and processing of organic light-emitting diodes*, CRC Press, 2015.
6 R.-P. Xu, Y.-Q. Li and J.-X. Tang, *J. Mater. Chem. C*, 2016, **4**, 9116–9142.
7 T. Tsujimura, *OLED display fundamentals and applications*, John Wiley & Sons, 2017.
8 J.-H. Jou, S. Kumar, A. Agrawal, T.-H. Li and S. Sahoo, *J. Mater. Chem. C*, 2015, **3**, 2974–3002.
9 J. L. Segura, *Acta Polym.*, 1998, **49**, 319–344.
10 J. Kido and Y. Okamoto, *Chem. Rev.*, 2002, **102**, 2357–2368.
11 C.-T. Chen, *Chem. Mater.*, 2004, **16**, 4389–4400.
12 K. T. Kamtekar, A. P. Monkman and M. R. Bryce, *Adv. Mater.*, 2010, **22**, 572–582.
13 D. Li, H. Zhang and Y. Wang, *Chem. Soc. Rev.*, 2013, **42**, 8416–8433.
14 M. Zhu and C. Yang, *Chem. Soc. Rev.*, 2013, **42**, 4963–4976.
15 D. Chen, S.-J. Su and Y. Cao, *J. Mater. Chem. C*, 2014, **2**, 9565–9578.
16 X. Yang, X. Xu and G. Zhou, *J. Mater. Chem. C*, 2015, **3**, 913–944.
17 M. Godumala, S. Choi, M. J. Cho and D. H. Choi, *J. Mater. Chem. C*, 2016, **4**, 11355–11381.
18 S. Laschat, A. Baro, N. Steinke, F. Giesselmann, C. Haegele, G. Scalia, R. Judele, E. Kapatsina, S. Sauer and A. Schreivogel, *Angew. Chem., Int. Ed.*, 2007, **46**, 4832–4887.
19 S. Sergeyev, W. Pisula and Y. H. Geerts, *Chem. Soc. Rev.*, 2007, **36**, 1902–1929.
20 B. R. Kaafarani, *Chem. Mater.*, 2010, **23**, 378–396.
21 R. J. Bushby and K. Kawata, *Liq. Cryst.*, 2011, **38**, 1415–1426.
22 M. O'Neill and S. M. Kelly, *Adv. Mater.*, 2011, **23**, 566–584.
23 S. Kumar, *Chemistry of discotic liquid crystals: from monomers to polymers*, CRC Press, 2016.
24 H.-W. Chen, J.-H. Lee, B.-Y. Lin, S. Chen and S.-T. Wu, *Light: Sci. Appl.*, 2018, **7**, 17168.
25 S. Kumar, *Chemistry of discotic liquid crystals: form monomers to polymers*, Taylor and Francis, CRC Press, Boca Raton, FL, 2011.
26 S. Kumar, *Chem. Soc. Rev.*, 2006, **35**, 83–109.
27 Y. Wang, Y. Liao, C. P. Cabry, D. Zhou, G. Xie, Z. Qu, D. W. Bruce and W. Zhu, *J. Mater. Chem. C*, 2017, **5**, 3999–4008.
28 M. Grell and D. D. Bradley, *Adv. Mater.*, 1999, **11**, 895–905.
29 A. E. Contoret, S. R. Farrar, P. O. Jackson, S. M. Khan, L. May, M. O'Neill, J. E. Nicholls, S. M. Kelly and G. J. Richards, *Adv. Mater.*, 2000, **12**, 971–974.
30 Y. Wang, J. Shi, J. Chen, W. Zhu and E. Baranoff, *J. Mater. Chem. C*, 2015, **3**, 7993–8005.
31 R. K. Gupta, D. Das, M. Gupta, S. K. Pal, P. K. Iyer and A. S. Achalkumar, *J. Mater. Chem. C*, 2017, **5**, 1767–1781.
32 A. K. Yadav, B. Pradhan, H. Ulla, S. Nath, J. De, S. K. Pal, M. N. Satyanarayan and A. S. Achalkumar, *J. Mater. Chem. C*, 2017, **5**, 9345–9358.

33 A. P. Sivadas, D. S. Rao, N. S. Kumar, D. D. Prabhu, S. Varghese, C. N. Ramachandran, R. M. Ongungal, S. Krishna Prasad and S. Das, *J. Phys. Chem. B*, 2017, **121**, 1922–1929.
34 Y. Wang, J. Shi, J. Chen, W. Zhu and E. Baranoff, *J. Mater. Chem. C*, 2015, **3**, 7993–8005.
35 D. Zhao, *Aggregation-Induced Emission: Materials and Applications*, ACS Publications, 2016, vol. 2, pp. 151–171.
36 T. N. Ahipa and A. V. Adhikari, *New J. Chem.*, 2014, **38**, 5018–5029.
37 T. N. Ahipa and A. V. Adhikari, *Photochem. Photobiol. Sci.*, 2014, **13**, 1496–1508.
38 T. N. Ahipa and A. V. Adhikari, *Tetrahedron Lett.*, 2014, **55**, 495–500.
39 T. N. Ahipa, V. Kumar, D. S. Rao, S. K. Prasad and A. V. Adhikari, *CrystEngComm*, 2014, **16**, 5573–5582.
40 D. R. Vinayakumara, H. Ulla, S. Kumar, A. Pandith, M. N. Satyanarayan, D. S. Rao, S. K. Prasad and A. V. Adhikari, *J. Mater. Chem. C*, 2018, **6**, 7385–7399.
41 S. Maruyama, K. Sato and H. Iwahashi, *Chem. Lett.*, 2010, **39**, 714–716.
42 H. Zheng, B. Xu and T. M. Swager, *Chem. Mater.*, 1996, **8**, 907–911.
43 J. Barberá, R. Giménez and J. L. Serrano, *Chem. Mater.*, 2000, **12**, 481–489.
44 L. Alvarez, J. Barberá, L. Puig, P. Romero, J. L. Serrano and T. Sierra, *J. Mater. Chem.*, 2006, **16**, 3768–3773.
45 A. Hayer, V. De Halleux, A. Köhler, A. El-Garoughy, E. W. Meijer, J. Barberá, J. Tant, J. Levin, M. Lehmann and J. Gierschner, *J. Phys. Chem. B*, 2006, **110**, 7653–7659.
46 E. Cavero, S. Uriel, P. Romero, J. L. Serrano and R. Giménez, *J. Am. Chem. Soc.*, 2007, **129**, 11608–11618.
47 C. V. Yelamaggad, A. S. Achalkumar, D. S. S. Rao and S. K. Prasad, *J. Mater. Chem.*, 2007, **17**, 4521–4529.
48 S. Kumar and S. K. Gupta, *Tetrahedron Lett.*, 2011, **52**, 5363–5367.
49 E. Beltrán, J. L. Serrano, T. Sierra and R. Giménez, *J. Mater. Chem.*, 2012, **22**, 7797–7805.
50 J. Tang, R. Huang, H. Gao, X. Cheng, M. Prehm and C. Tschierske, *RSC Adv.*, 2012, **2**, 2842–2847.
51 T. Wöhrle, I. Wurzbach, J. Kirres, A. Kostidou, N. Kapernaum, J. Litterscheidt, J. C. Haenle, P. Staffeld, A. Baro and F. Giesselmann, *Chem. Rev.*, 2015, **116**, 1139–1241.
52 S. Park and B.-K. Cho, *Soft Matter*, 2015, **11**, 94–101.
53 R. K. Konidena, K. J. Thomas, M. Singh and J.-H. Jou, *J. Mater. Chem. C*, 2016, **4**, 4246–4258.
54 S. Sasaki, G. P. Drummen and G. Konishi, *J. Mater. Chem. C*, 2016, **4**, 2731–2743.
55 W. Li, D. Liu, F. Shen, D. Ma, Z. Wang, T. Feng, Y. Xu, B. Yang and Y. Ma, *Adv. Funct. Mater.*, 2012, **22**, 2797–2803.
56 S. Zhang, W. Li, L. Yao, Y. Pan, F. Shen, R. Xiao, B. Yang and Y. Ma, *Chem. Commun.*, 2013, **49**, 11302–11304.
57 S. Zhang, L. Yao, Q. Peng, W. Li, Y. Pan, R. Xiao, Y. Gao, C. Gu, Z. Wang and P. Lu, *Adv. Funct. Mater.*, 2015, **25**, 1755–1762.
58 A. K. Yadav, B. Pradhan, H. Ulla, S. Nath, J. De, S. K. Pal, M. N. Satyanarayan and A. S. Achalkumar, *J. Mater. Chem. C*, 2017, **5**, 9345–9358.
59 R. K. Gupta, H. Ulla, M. N. Satyanarayan and A. A. Sudhakar, *Eur. J. Org. Chem.*, 2018, 1608–1613.
60 H. Ulla, M. Raveendra Kiran, B. Garudachari, M. N. Satyanarayan, G. Umesh and A. M. Isloor, *Opt. Mater.*, 2014, **37**, 311–321.
61 H. Ulla, M. R. Kiran, B. Garudachari, T. N. Ahipa, K. Tarafder, A. V. Adhikari, G. Umesh and M. N. Satyanarayan, *J. Mol. Struct.*, 2017, **1143**, 344–354.
62 S. Chidirala, H. Ulla, A. Valaboju, M. R. Kiran, M. E. Mohanty, M. N. Satyanarayan, G. Umesh, K. Bhanuprakash and V. J. Rao, *J. Org. Chem.*, 2016, **81**, 603–614.
63 J. Tagare, H. Ulla, M. N. Satyanarayan and S. Vaidyanathan, *J. Photochem. Photobiol., A*, 2018, **353**, 53–64.
64 J. Tagare, H. Ulla, M. N. Satyanarayan and S. Vaidyanathan, *J. Lumin.*, 2018, **194**, 600–609.
65 J. Tagare, H. Ulla, A. B. Kajjam, M. N. Satyanarayan and S. Vaidyanathan, *ChemistrySelect*, 2017, **2**, 2611–2620.

